

SPE-213359-MS

Application of Image Processing Techniques in Deep-Learning Workflow to Predict CO₂ Storage in Highly Heterogeneous Naturally Fractured Reservoirs: A Discrete Fracture Network Approach

Zeeshan Tariq, Bicheng Yan, and Shuyu Sun, King Abdullah University of Science and Technology

Copyright 2023, Society of Petroleum Engineers DOI [10.2118/213359-MS](https://doi.org/10.2118/213359-MS)

This paper was prepared for presentation at the Middle East Oil, Gas and Geosciences Show held in Manama, Bahrain, 19 – 21 February 2023. The official proceedings were published online on 7 March 2023.

This paper was selected for presentation by an SPE program committee following review of information contained in an abstract submitted by the author(s). Contents of the paper have not been reviewed by the Society of Petroleum Engineers and are subject to correction by the author(s). The material does not necessarily reflect any position of the Society of Petroleum Engineers, its officers, or members. Electronic reproduction, distribution, or storage of any part of this paper without the written consent of the Society of Petroleum Engineers is prohibited. Permission to reproduce in print is restricted to an abstract of not more than 300 words; illustrations may not be copied. The abstract must contain conspicuous acknowledgment of SPE copyright.

Abstract

Naturally fractured reservoirs (NFRs), such as fractured carbonate reservoirs, are commonly located worldwide and have the potential to be good sources of long-term storage of carbon dioxide (CO₂). The numerical reservoir simulation models are an excellent source for evaluating the likelihood and comprehending the physics underlying behind the interaction of CO₂ and brine in subsurface formations. For various reasons, including the rock's highly fractured and heterogeneous nature, the rapid spread of the CO₂ plume in the fractured network, and the high capillary contrast between matrix and fractures, simulating fluid flow behavior in NFR reservoirs during CO₂ injection is computationally expensive and cumbersome. This paper presents a deep-learning approach to capture the spatial and temporal dynamics of CO₂ saturation plumes during the injection and monitoring periods of Geological Carbon Sequestration (GCS) sequestration in NFRs. To achieve our purpose, we have first built a base case physics-based numerical simulation model to simulate the process of CO₂ injection in naturally fractured deep saline aquifers. A standalone package was coded to couple the discrete fracture network in a fully compositional numerical simulation model. Then the base case reservoir model was sampled using the Latin-Hypercube approach to account for a wide range of petrophysical, geological, reservoir, and decision parameters. These samples generated a massive physics-informed database of around 900 cases that provides a sufficient training dataset for the DL model. The performance of the DL model was improved by applying multiple filters, including the Median, Sato, Hessian, Sobel, and Meijering filters. The average absolute percentage error (AAPE), root mean square error (RMSE), Structural similarity index metric (SSIM), peak signal-to-noise ratio (PSNR), and coefficient of determination (R²) were used as error metrics to examine the performance of the surrogate DL models. The developed workflow showed superior performance by giving AAPE less than 5% and R² more than 0.94 between ground truth and predicted values. The proposed DL-based surrogate model can be used as a quick assessment tool to evaluate the long-term feasibility of CO₂ movement in a fracture carbonate medium.

Keywords: Naturally fractured reservoirs, deep learning, image processing, Fourier Neural Operator, discrete fracture network

Introduction

A carbonate reservoir is defined as being "fractured" only if a continuous network of various degrees of fracturing is distributed throughout the reservoir (Warren and Root, 1963). Such fractures formed naturally during the specific geological circumstances of reservoir history (Cinco-Ley and Fernando Samaniego, 1981). Naturally Fractured Reservoirs (NFR) are represented by two types of porous and permeable media: fractures & matrix. In such reservoir systems, the fluid flow is from matrix and fractures, while in dual porosity single permeability reservoirs, the fluid flow is from fractures only. Because of the unique conductivity and fluid storage characteristic of fractures and matrix, these reservoirs are usually called dual-porosity/dual permeability reservoirs (Qasem et al., 2014; Sadeghi et al., 2013; Saidi, 1983). The matrix provides major storage, while fractures provide the principal passage for the fluid flow (Cheng, 1990; Dean and Lo, 1988; Tariq et al., 2018b, 2016). Fractured reservoir systems vary vastly compared to simple single-porosity techniques, as not only should the dual porosity/dual permeability continuum be considered, but even the processes involved in the transfer between the two systems are essential in understanding these complex structures. Considering these complexities, model efforts have been made several years ago (Cinco-Ley and Fernando Samaniego, 1981; Retnanto and Economides, 1998). The amount of heterogeneity and anisotropy incorporated in NFRs presents a challenge starting right from reservoir characterization and including the production strategies; hence it is imperative to know the future performance of such reservoirs to plan all the activities from drilling to completion and facilities design.

Underground storage of carbon dioxide is considered one of the most imperative needs of the current era to reduce the release of anthropogenic greenhouse gas emissions into the atmosphere (Fatima et al., 2021; Tariq et al., 2018a). Reducing the worst impact of greenhouse gases on the atmosphere and the initiatives towards net zero carbon neutral energy options have been the core attention over the past many years across the globe (Nguyen, 2003; Rosenbauer et al., 2005). The world population has been continually increasing, which consequently increases energy demand, and subsequently, the world will not peak in utilizing energy shortly (Mohapatra et al., 2019; Rosenbauer et al., 2005; Vanorio et al., 2011). This has triggered collaborative discussions among hydrocarbon peers to address the risks of climate action on business sustainability, as greenhouse gases are the primary concerns for global warming and climate change (Aminu et al., 2017; Chen et al., 2020, 2018; Michael et al., 2010; Sharma, 2011a, 2011b; Viebahn et al., 2015a, 2015b; Zhou et al., 2016). Geological Carbon Sequestration (GCS) into a deep subterranean formation, like saline aquifers, unminable coal seams, and depleted hydrocarbon reservoirs, brings enormous potential for large-scale storage of carbon dioxide (Alam et al., 2014; Egermann et al., 2005; Grigg and Svec, 2006; Moghadasi et al., 2004; Mohamed and Nasr-El-Din, 2012). Among all the storage sites, saline aquifers are the most attractive candidate site because of the large pore volume for storage, but it requires high capital investment in drilling new wells and conducting seismic surveys for long-term storage assessments (Keating et al., 2016). The successful implementation of GCS requires a comprehensive risk assessment of the confinement of plumes at each potential storage site (Cook et al., 2014; Keating et al., 2016; Pawar et al., 2014; Shabani and Vilcáez, 2018). The accurate prediction of the flow, geochemical, and geomechanical responses of the formation is essential for the management of GCS in long-term operations because excessive pressure buildup due to injection can potentially induce fracturing of the cap-rock, or activate pre-existing faults, through which fluid can leak. The geological media to store CO₂ for a more extended period must have sufficient capacity, and injectivity must confine or at least delay the vertical migration of injected CO₂ due to the gravity effects.

Naturally fractured reservoirs (NFR) are present worldwide and potentially excellent sources of storing carbon dioxide (CO₂) for extended periods. The numerical simulation models are excellent tools to evaluate the long-term storage potential of CO₂ in such reservoirs, eventually helping better to understand the physics behind CO₂-brine interaction in subsurface reservoirs. Simulating the behavior of fluid flow in NFR reservoirs during CO₂ is computationally expensive for multiple reasons, such as the highly-fractured and

heterogeneous nature of the rock, fast propagation of CO₂ plume in the fracture network, and high capillary contrast between matrix and fractures. In this study, we have built a Deep Learning (DL) workflow to effectively infer the storage potential of CO₂ in deep saline aquifers. The DL workflow-based surrogate model to predict saturation inputs porosity, Permeability, injection rate, perforation depth, salinity, reservoir temperature, reservoir thickness, and discrete time steps.

Methodology

This section describes governing equations, reservoir models, initial reservoir conditions, rock properties, and injection schemes. We have used the commercial numerical simulator CMG-GEM (Add a reference of CMG) to develop the multiphase flow data set for CO₂ geological storage.

Numerical Model Description

This section describes the numerical simulation model. In this study, we have run multiple simulations using a compositional numerical simulator (Computer Modeling Group CMG-GEM) to generate the multiphase flow data. CMG-GEM is an advanced complete physics, multi-component flow, transport, and numerical heat simulator using a finite difference simulation method. CMG-GEM uses equation-of-states (EOS) to calculate the fluid properties and several rock-fluid correlations to calculate rock properties such as relative Permeability and capillary pressures. CMG-GEM can also be coupled with finite-element geomechanical modules with non-plastic and plastic strains.

The physical model comprised a single well located at the center of the reservoir. The classical carbonate reservoir is considered in this study to establish the DL workflow. Table 1 shows the reservoir model parameters used in the numerical modeling. Table 2 shows the critical parameters properties of the H₂O and CO₂. We have injected supercritical CO₂ at a constant rate through a vertical injection well with a radius of 0.076 m. The well was perforated over the selected depth of interval. We have simulated the injection of supercritical CO₂ for 30 years at a constant rate ranging from 0.5 to 5 MT/year and monitored the movement of the CO₂ plume for the next 170 years. The outer boundary is closed but is sufficiently distant from the injection well that it behaves like an infinite-acting reservoir. The reservoir section has an initial pressure of 24000 KPa.

Table 1—Reservoir Simulation Input for base case model

Reservoir Parameters	Values	Units
Reservoir Thickness	20-200	m
Reservoir Depth at the top of the formation	2400	m.
Initial Reservoir pressure	25888.4	KPa
Reservoir Lithology	Limestone	
Rock Compressibility	3×10^{-6}	psi ⁻¹
Porosity	25	%
Initial Reservoir Temperature	80	°C
Aquifer Salinity	57000	ppm
Dykstra-Parsons Coefficient	0.6	
Average Horizontal Permeability kh	220	mD
Vertical Permeability	0.1 * kh	mD
No. of Injection Well	1	
Well diameter	0.375	ft.
Aquifer water density	1020	Kg/m ³
Injection rate	1×10^6	m ³ /day

Reservoir Parameters	Values	Units
Maximum Injection Pressure	50000	KPa

Table 2—Critical Properties of CO₂

Components	H ₂ O	CO ₂	Units
Critical Pressure	220.6	73.8	Bar
Critical Temperature	373.94	30.98	°C
Critical Volume	0.056	0.094	liter/g-mol
Molecular Weight	18.015	44	g/g-mol
Acentric factor	0.344	0.22394	—
Parachor	52	78	—

The fluid phases in a saline aquifer CO₂ sequestration include aqueous and supercritical phases. The mass balance equation for the flow and transport equation of CO₂ storage is given by Eq. 1

$$\frac{\partial}{\partial t} \left(\phi \sum_{\alpha} S_{\alpha} \rho_{\alpha} x_{\alpha i} \right) - \nabla \cdot \left\{ K \sum_{\alpha} \frac{k_{r\alpha}}{\mu_{\alpha}} \rho_{\alpha} x_{\alpha i} (\nabla p_{\alpha} + \rho_{\alpha} g \nabla Z) \right\} + \sum_l \left(\sum_{\alpha} \rho_{\alpha} x_{\alpha i} q_{\alpha} \right)^l \quad (1)$$

where, the first term denotes the fluid accumulation, the second term is the advective flux based on Darcy's law; and the third term is the source or sink term. The subscript i denotes the primary fluid components, including CO₂ and water; α denotes the fluid phases, including water and CO₂; t is the time; ϕ is the porosity; S_{α} is the phase saturation; ρ_{α} is the fluid phase density; $x_{\alpha i}$ is the mole fraction of component i in the fluid phase α ; k is the Permeability; $k_{r\alpha}$ is the phase relative permeability; μ_{α} is the phase viscosity; p_{α} is the pressure of the fluid; g is the gravity; Z is the depth; q_{α} is the denotes the rate for producing or injecting fluid phase through well perforation l . During the GCS project, supercritical phase CO₂ is injected into the deep saline aquifers which was previously occupied with saline water. Therefore, two-phase (aqueous and supercritical phases) relative permeability is a key parameter to determine the effective Permeability of each phase. In this study, (Brooks & Corey, 1964) correlation is used to model the relative Permeability of supercritical CO₂ and brine system.

$$k_{rw} = \overline{S}_w^{(3+2/\lambda)} \quad (2)$$

$$k_{rg} = \overline{S}_g \left(1 - (1 - \overline{S}_g)^{(1+2/\lambda)} \right) \quad (3)$$

$$\overline{S}_w = \frac{S_w - S_{wi}}{1 - S_{gi} - S_{wi}} \quad (4)$$

$$\overline{S}_g = \frac{S_g - S_{gi}}{1 - S_{gi} - S_{wi}} \quad (5)$$

λ is the pore size distribution index, where k_{rw} is the relative Permeability of the water phase, k_{rg} is the relative Permeability of the supercritical CO₂ phase, S_{wi} is the irreducible water saturation, S_{gi} is the irreducible gas saturation. Figure 1 shows the gas-brine relative permeability curve used in this study. The effect of pore sizes are not very much significant so that a constant value of $\lambda = 3$ is used in all cases.

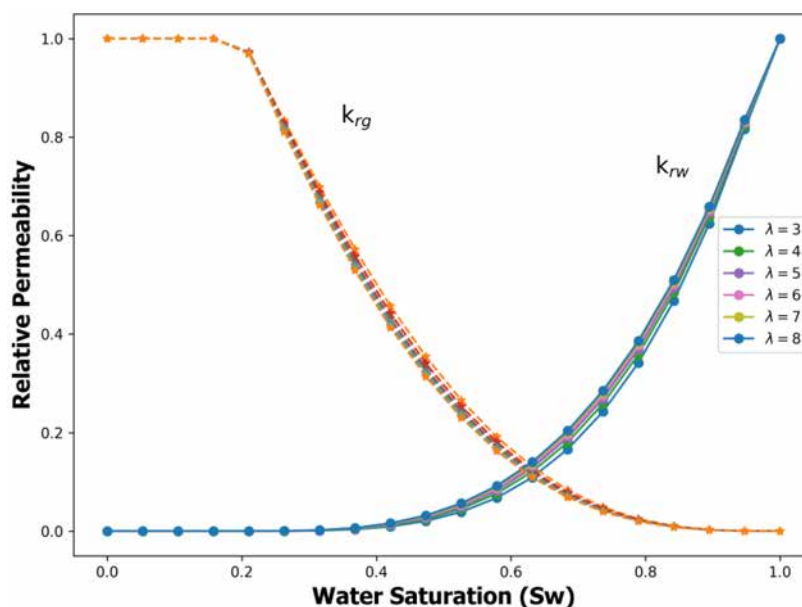


Figure 1—Gas and brine relative permeability curves were obtained after varying the pore size distribution between 3 – 8.

DFN Model

This work applied an upscaling-based algorithm to generate random fracture distribution and incorporate fracture into a matrix. The discrete fracture networks (DFNs) are developed stochastically, and the single fractures are assumed to be a straight line in 2D maps (Lei et al. 2017). There are some random features included in both fracture and matrix. The fracture properties such as Permeability (κ_f), porosity (ϕ_f), orientation (θ) are selected uniformly within a given range and applied to every single fracture, while the fracture lengths follow the lognormal distribution and the fracture location are distributed stochastically. A slight heterogeneity was used to matrix porosity (ϕ_m) and Permeability (κ_m), both two variables follow Gaussian random distribution modeling by GStools (Müller et al. 2022). Upscaling DFNs to general reservoir flow simulation model based on grid blocks are implemented and assessed in literature (Ahmed Elfeel and Geiger 2012, Hyman et al. 2015, Sherratt et al. 2020), the connections of fracture can be removed incorrectly when the upscaling is based on a corner-point grid or Cartesian grid, which may lead the deduction of transmissibility at grid face and erroneously block fluid flow and propagation. Figure 2 shows the number of fractures obtained from the developed DFN model.

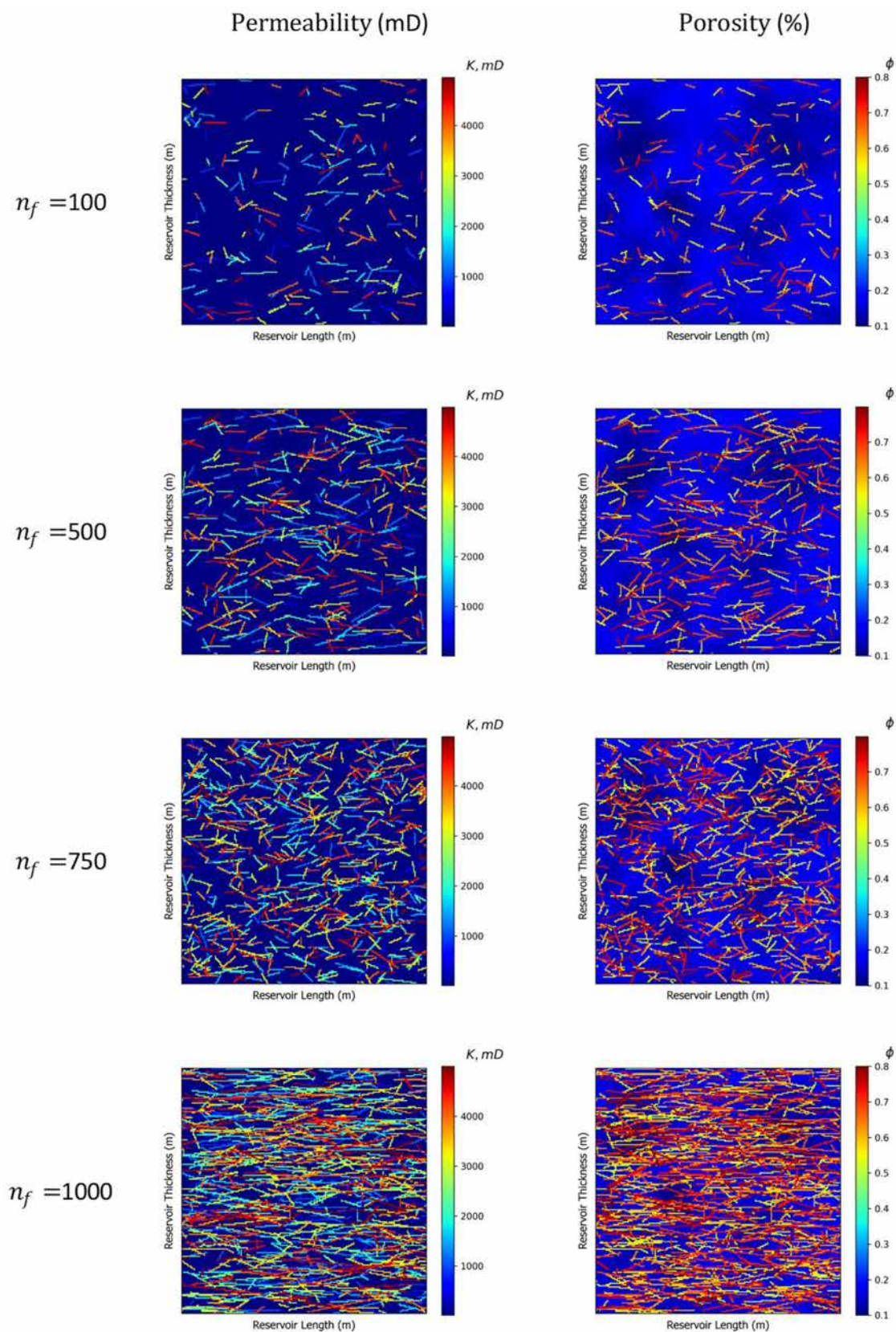


Figure 2—Examples of the varied number of fractures in the numerical reservoir simulator.

Deep Learning Model

In this study, Fourier Neural Operators are used to monitor the movement of the CO₂ plume. The architecture of *FNO* is based on image-based convolutional neural networks, which have already been demonstrated to predict state variables following spatial-temporal patterns in our previous work (Yan et al., 2022). Here we adopt the 2D Fourier Neural Operator (FNO) (Li et al. 2020) as it has been validated with the great capacity to predict different PDE-based problems (Burger's Equation, Darcy equation, and Navier-Stokes equation). The architecture of FNO is presented in Figure 3.

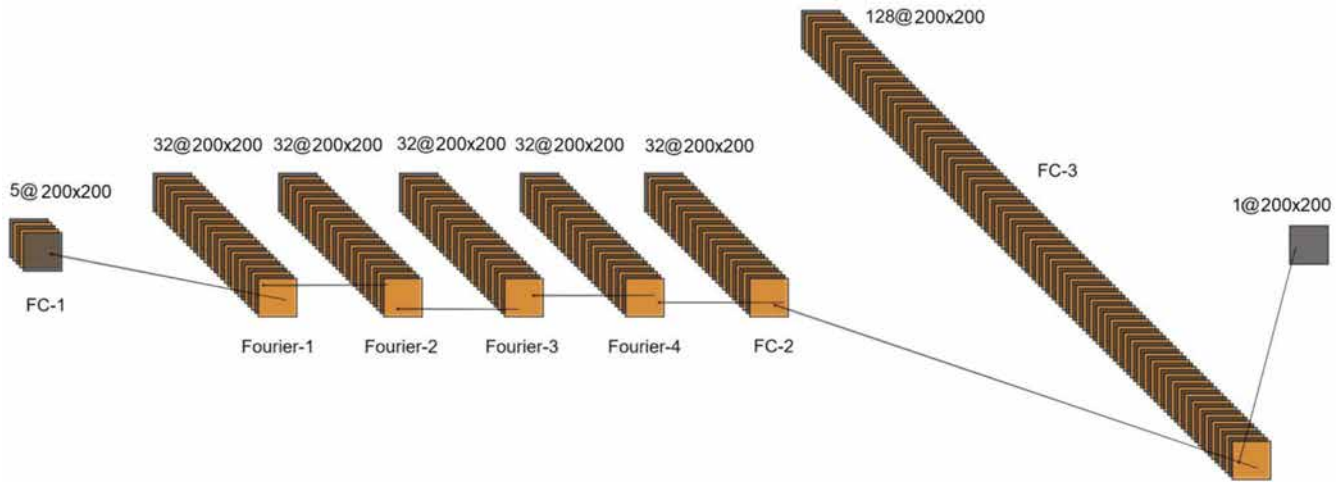


Figure 3—The architecture of Fourier Neural Operator with four Fourier layers and three fully connected layers.

The input X is transformed into V_0 in a certain higher-dimensional space through a fully connected layer (FC-1), and further iterates through multiple Fourier layers by updating as Eq. 7

$$V_l = \sigma(WV_{l-1} + \mathcal{K}(V_{l-1})), l = 1, \dots, L \quad (6)$$

where, σ denotes the nonlinear activation function, and here we use rectified linear unit function (ReLU); W is a linear operator defined by a 1D convolutional operator; K is a 2D convolution operator defined in the Fourier space.

Ultimately V_L is converted to the state variable mineral η via two fully connected layers (FC-2 and FC-3). The loss function to train f_l is represented as Equation (8),

$$\mathcal{L}_{f_l}(\theta_l) = \|X - \hat{X}\| \quad (7)$$

Where $\mathcal{L}_{f_l}(\theta_l)$ denotes the loss function of f_l ; θ_l are the learnable parameters in f_l ; $\|\cdot\|$ is a root-mean-square-error operator; X is the true solution of minerals; \hat{X} denotes the prediction of Y . The goal of training is to find θ_l^* by minimizing $\mathcal{L}_{f_l}(\theta_l)$, shown as,

$$\theta_l^* = \operatorname{argmin}_{\theta_l}(\mathcal{L}_{f_l}(\theta_l)) \quad (8)$$

The Adam optimizer (Kingma and Ba 2014) is applied to train f_c , with learning rate 10^{-4} and weight decay 10^{-4} . Finally, we remark that f_h is a non-differentiable physics-based numerical model, while f_l is a fully automatically differentiable neural network model.

The root mean squared error (RMSE), average absolute percentage error (AAPE), and coefficient of correlation (CC) were determined for the predicted values to evaluate the accuracy and reliability of the models. Mathematical relations of AAPE, RMSE, CC, and R^2 are given in Eq. 10 – 13.

$$AAPE = \frac{\sum |(\beta_{\text{true}} - \beta_{\text{predicted}})| * \frac{100}{\beta_{\text{true}}}}{n_{\text{samples}}} \quad (9)$$

$$RMSE = \sqrt{\frac{\sum (\beta_{\text{true}} - \beta_{\text{predicted}})^2}{n_{\text{samples}}}} \quad (10)$$

$$CC = \frac{\sum (x_i - \bar{x})(y_i - \bar{y})}{\sqrt{\sum (x_i - \bar{x})^2 \sum (y_i - \bar{y})^2}} \quad (11)$$

$$R^2 = \left(\frac{\sum (x_i - \bar{x})(y_i - \bar{y})}{\sqrt{\sum (x_i - \bar{x})^2 \sum (y_i - \bar{y})^2}} \right)^2 \quad (12)$$

Where x and y are two variables, and n is the number of samples.

The peak signal-to-noise ratio (PSNR) is given by Eq. 14.

$$PSNR = 10 \log_{10} \frac{(L-1)^2}{MSE} = 20 \log_{10} \frac{L-1}{RMSE} \quad (13)$$

Here, L is the number of maximum possible intensity levels (minimum intensity level supposed to be 0) in an image.

The structural similarity index (SSIM) was calculated to evaluate the performance of the models. SSIM calculates the difference between ground truth and predicted image by moving pixels across the images. The Equation to calculate SSIM is given by Eq. 11.

$$SSIM(u, v) = \frac{1}{M} \sum_{m=1}^M \frac{(2\mu_{u,m}\mu_{v,m} + K_1)(2\sigma_{uv,m} + K_2)}{(\mu_{u,m}^2 + \mu_{v,m}^2 + K_1)(\sigma_{u,m}^2 + \sigma_{v,m}^2 + K_2)} \quad (14)$$

Where u and v are, respectively, the true and the predicted values (images). The SSIM is computed in M local windows in the images of u and v ; μ denotes the mean, and σ represents the standard deviation; K_1 and K_2 are small constants to avoid zero values in the denominator terms of Eq. 14. The minimum value of SSIM is '0', representing noisy images, while the maximum value of '1' represents an actual image.

Results and Discussions

The base case model was sampled by varying several uncertain parameters. A total of six parameters were varied, including Permeability, porosity, injection rate, perforation thickness, temperature, salinity, and reservoir thickness. The Latin Hypercube sampling approach was used to design numerical experiments. To reduce the number of variables, injection rate and perforation thickness were combined as one variable. Figure 4 shows the combined injection rate and perforation depth as a single variable.

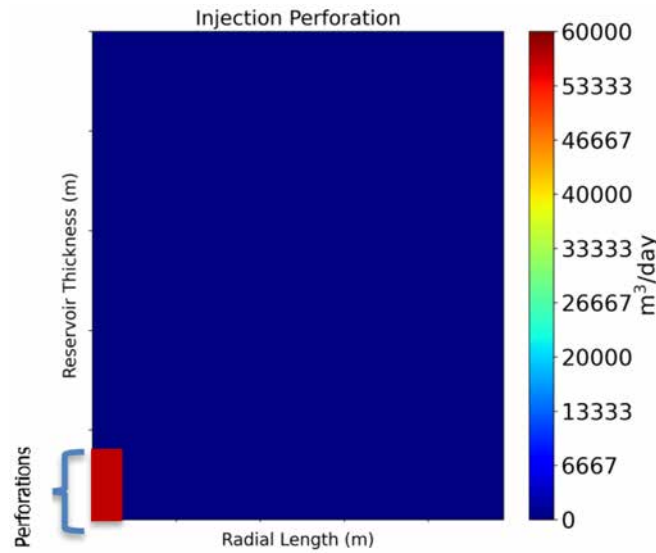


Figure 4—Combined injection rate and perforation depth as a parameter.

Permeability and porosity were converted into a single variable named reservoir quality index (RQI) to reduce input features further. RQI was calculated by taking the ratio of Permeability and porosity. RQI was calculated by Eq. (15).

$$RQI = \sqrt{\frac{k}{\phi}} \quad (15)$$

Nine hundred simulations were performed for 45 discrete time steps on 200 by 200 domain sizes. In terms of images, we have generated $900 \times 45 = 40500$ images. The training dataset was 80% of the whole data, while the testing and validation datasets were 10% each. Therefore, 720 cases or $720 \times 45 = 32400$ images were used for the training, 4050 images were used for testing, and 4050 images were used for validation. In order to reproduce the same result, the torch seed command was implemented inside the code. Figure 5 shows one of the cases with static input parameters, including Permeability, porosity, RQI, and injection perforation. Figure 6 shows the cross plot between ground truth simulation saturation and FNO predicted saturation. The R^2 between ground truth and FNO predicted saturation on a validation dataset was found to be 0.875.

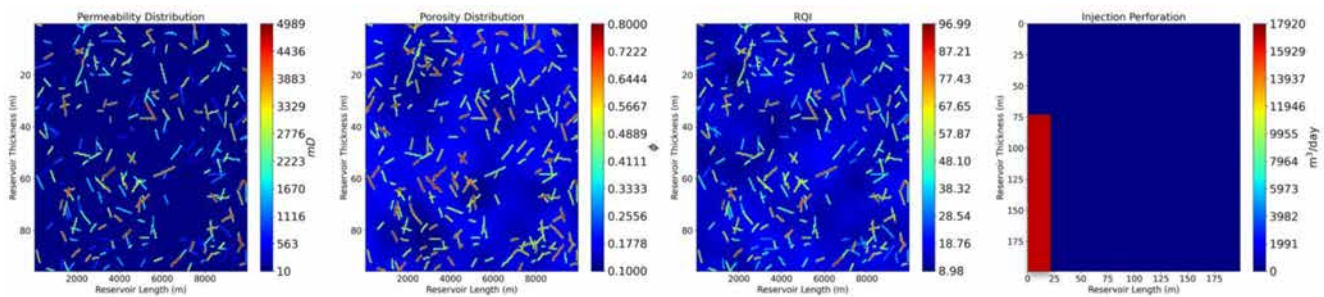


Figure 5—Examples of the dataset used for the training of the deep learning model. From left to right, Permeability, porosity, reservoir quality index (RQI), and perforation-injection rate. Examples shown over here are for the case199.

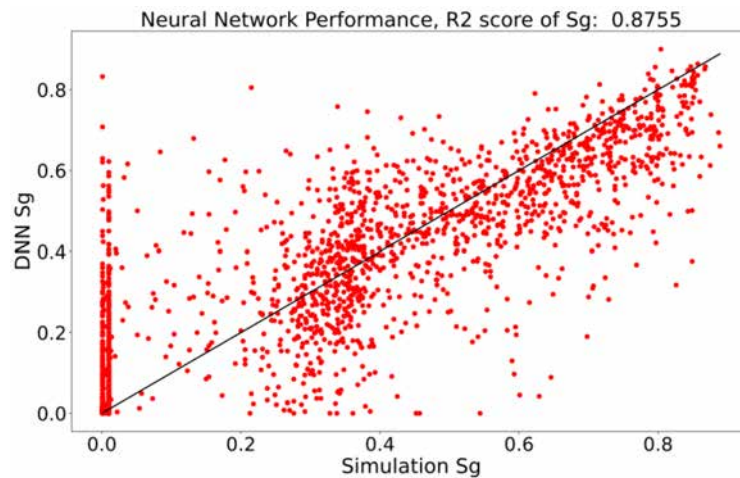


Figure 6—DNN predicted and CMG-based gas saturation.

To improve the prediction accuracy, we have used five different filters on the RQI dataset. These filters include Median, Sobel, Hessian, Sato, and Meijering. Each filter was applied to improve the topological and textural information of the image. Figure 7 shows the implementation of these five filters on the RQI dataset. The first filter we implemented was the Median filter. The median filter is a nonlinear digital filtering technique primarily used to eliminate noise from an image while preserving the edges. The second filter is the Sobel edge detector, which computes the absolute non-directional pixel-intensity gradient at each pixel by applying an 3×3 edge-detection matrix. The Sobel filter technique detects irregular edges in the image. This process allows the Sobel filter to compute vertical and horizontal edges. Like the Sobel edge detector, the Hessian filter describes the second-order pixel-intensity variations. The hessian filter detects even edges. The filter can see edges and corner regions based on the calculated eigenvalues. Next is the Sato filter, referred to as the tubeness filter. The Sato filter detects continuous ridges by calculating the Hessian matrix's eigenvectors and then computing an image's similarity to tubes. The fifth filter is the Meijering filter. A meijering filter is often used to detect continuous wrinkle ridges and unconformities. The meijering filter calculates the Hessian's eigenvectors to compute the similarity of an image region to neurites. The histograms of each filter applied on the RQI dataset are shown in Figure 8.

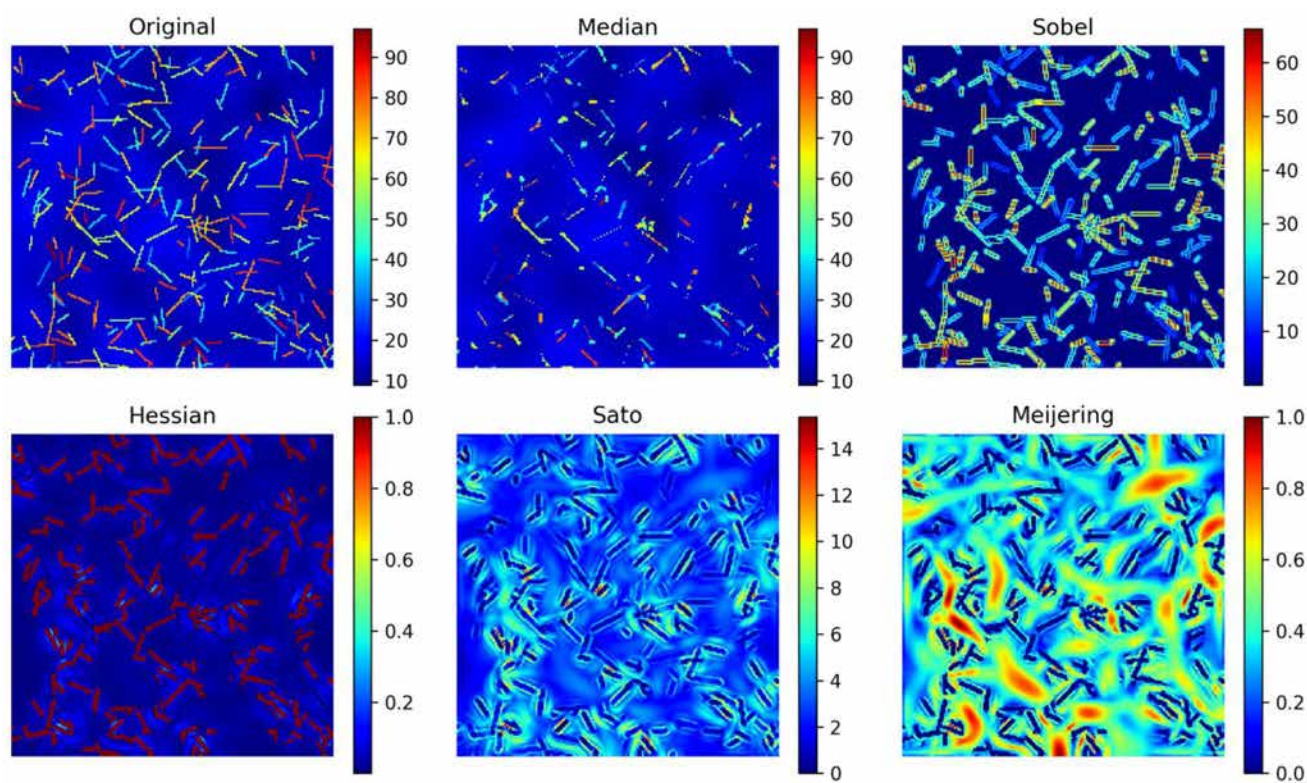


Figure 7—View of five filters applied on RQI dataset.

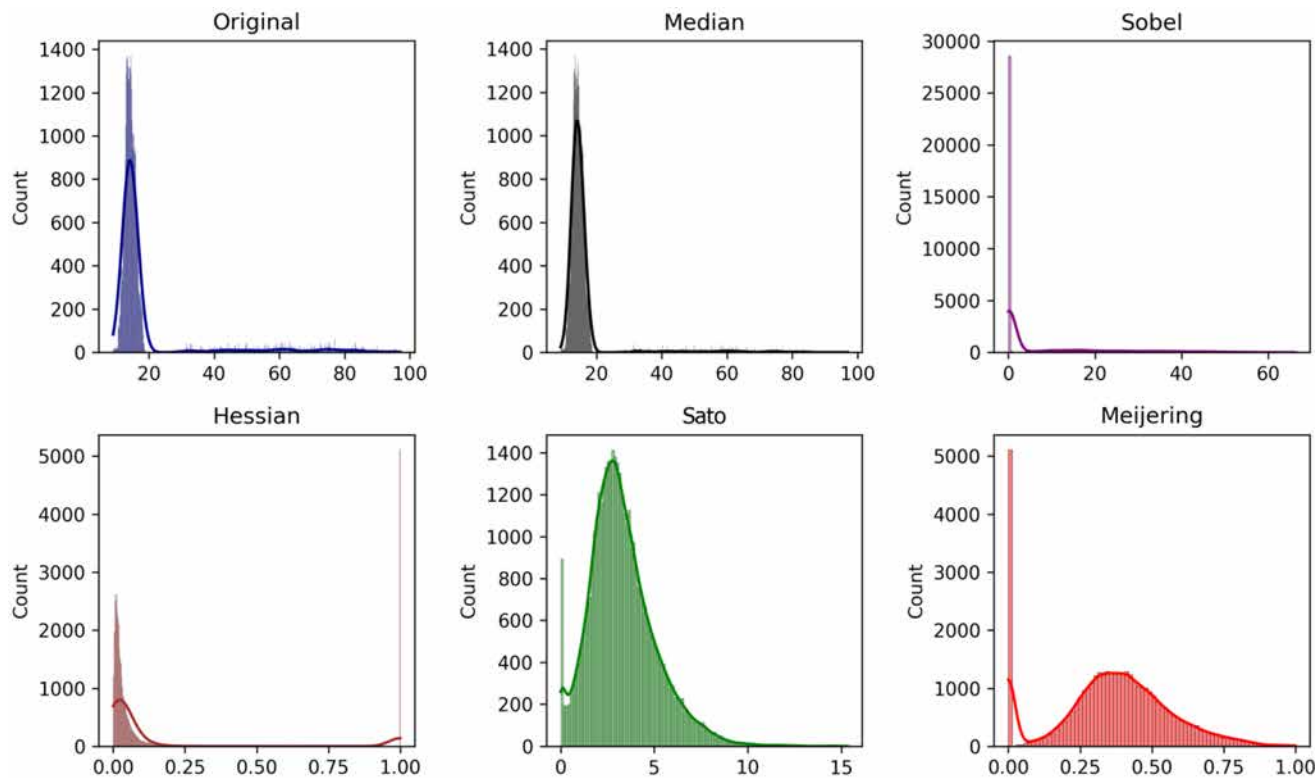


Figure 8—Comparison of histograms of the filtered images.

After applying five filters to the RQI dataset, the filtered images were also used as input features to predict the saturation of CO₂. With a new set of input parameters and using the same FNO architecture, as shown in Figure 3, the prediction accuracy improved to 0.90. The total inputs increased to ten, including RQI, RQI-Median, RQI-Sobel, RQI-Hessian, RQI-Sato, RQI-Meijering, reservoir temperature, injection-perforation, aquifer salinity, and reservoir thickness.

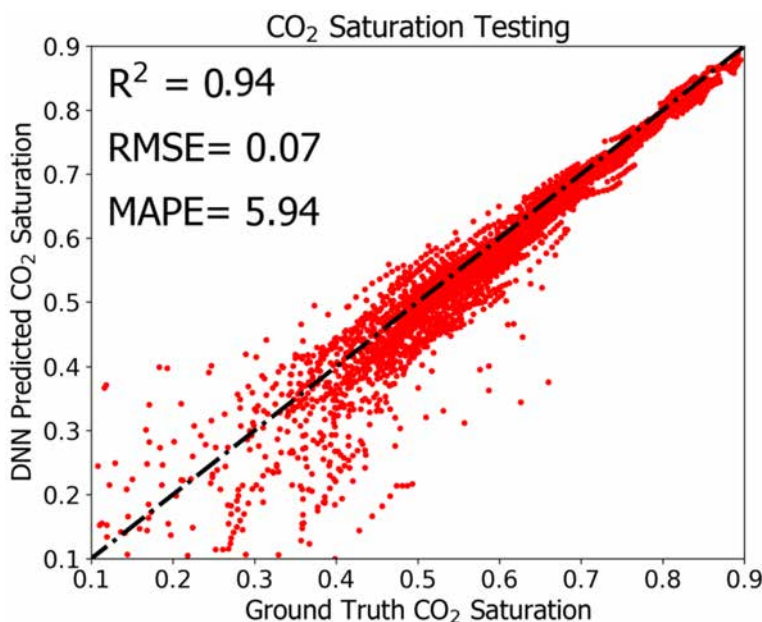
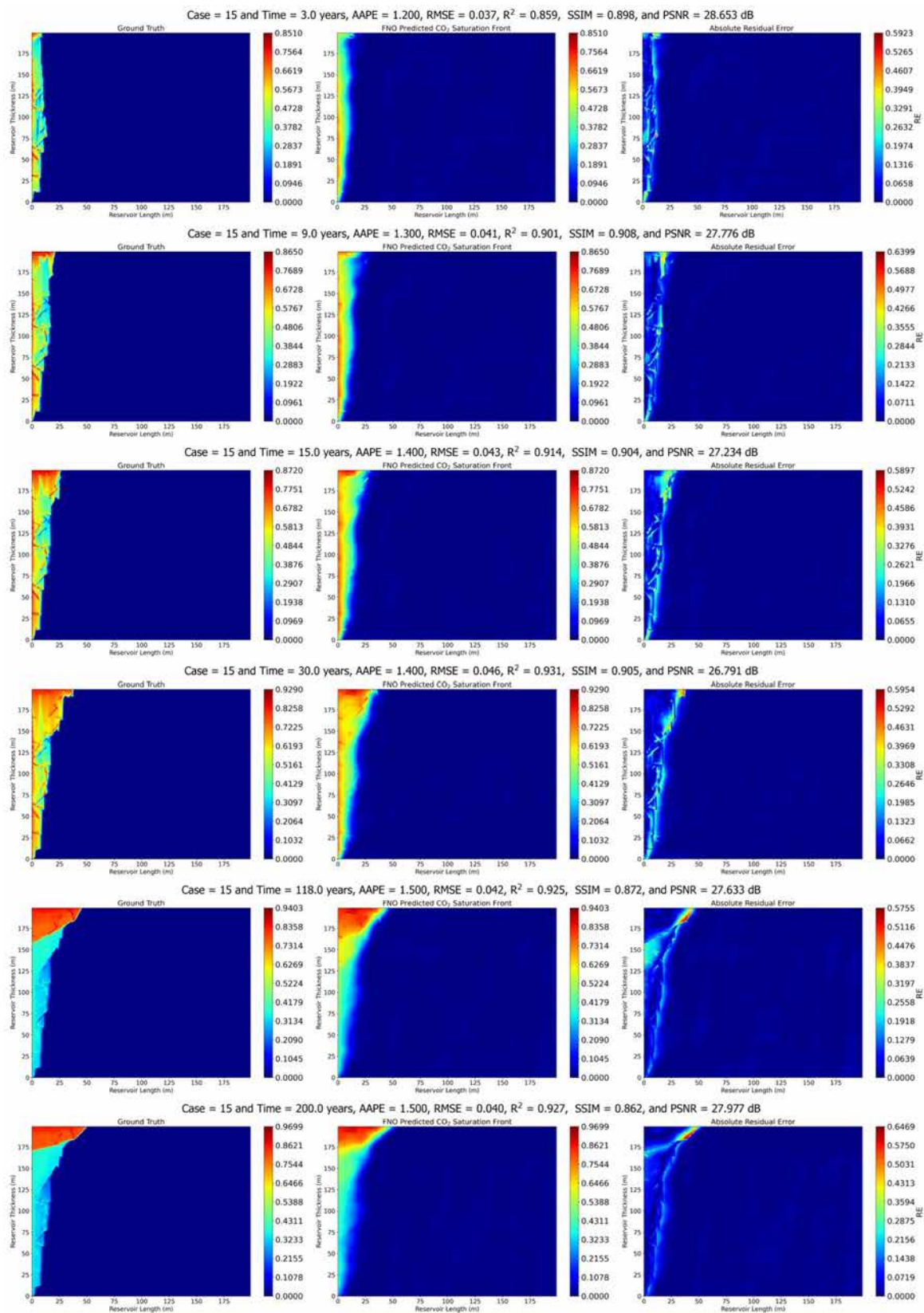


Figure 9—The testing cross-plot between actual and predicted values of CO₂ saturation.

Figure 10 shows the ground truth from the simulator, DNN predicted values, and absolute difference error between actual and predicted values. AAPE, RMSE, SSIM, and PSNR were calculated for all the cases. The results of the randomly selected case, 15 are shown. In each case for saturation prediction, six discrete time intervals are chosen to compare the DNN models performances, including the 3 years, 9 years, 15 years, 30 years, 118 years, and 200 years. The performance of the DNN model in predicting CO₂ saturation in NFR reservoirs were quite excellent by giving less errors and higher SSIM.



Conclusions

In this study, we have developed a DL workflow to effectively predict temporal-spatial prediction of saturation during CO₂ storage in naturally fractured deep saline aquifers. Based on the results and discussions following conclusions can be drawn:

1. FNO predicted the saturation of CO₂ gas as a function of reservoir quality index, injection rate, perforation depth, salinity, temperature, and thickness.
2. FNO can predict the saturation of CO₂ gas in naturally fractured deep saline aquifers with an accuracy of 0.875 in terms of R².
3. The prediction accuracy of the FNO model was increased by applying different filters on the RQI dataset.
4. In terms of R², filters have improved the accuracy to 0.94 from 0.875

References

- Ahmed Elfeel Mohamed and Geiger, Sebastian. 2012. Static and dynamic assessment of DFN permeability upscaling. *Proc., SPE Europe/EAGE Annual Conference*.
- Alam, M.M., Hjuler, M.L., Christensen, H.F., Fabricius, I.L., 2014. Petrophysical and rock-mechanics effects of CO₂ injection for enhanced oil recovery: Experimental study on chalk from South Arne field, North Sea, in: *Journal of Petroleum Science and Engineering*. Society of Petroleum Engineers, pp. 468–487. <https://doi.org/10.1016/j.petrol.2014.08.008>
- Aminu, M.D., Nabavi, S.A., Rochelle, C.A., Manovic, V., 2017. A review of developments in carbon dioxide storage. *Appl Energy* **208**, 1389–1419. <https://doi.org/10.1016/J.APENERGY.2017.09.015>
- Chen, B., Harp, D.R., Lin, Y., Keating, E.H., Pawar, R.J., 2018. Geologic CO₂ sequestration monitoring design: A machine learning and uncertainty quantification based approach. *Appl Energy* **225**, 332–345. <https://doi.org/10.1016/j.apenergy.2018.05.044>
- Chen, B., Harp, D.R., Lu, Z., Pawar, R.J., 2020. Reducing uncertainty in geologic CO₂ sequestration risk assessment by assimilating monitoring data. *International Journal of Greenhouse Gas Control* **94**, 102926. <https://doi.org/10.1016/j.ijggc.2019.102926>
- Cheng, A.M., 1990. Inflow performance relationships for solution-gas-drive slanted/horizontal wells, in: *Proceedings – SPE Annual Technical Conference and Exhibition*. Society of Petroleum Engineers, pp. 77–84. <https://doi.org/10.2523/20720-ms>
- Cinco-Ley, H., Fernando Samaniego, V., 1981. Transient pressure analysis: Finite conductivity fracture case versus damaged fracture case, in: *Proceedings – SPE Annual Technical Conference and Exhibition*. Society of Petroleum Engineers. <https://doi.org/10.2523/10179-ms>
- Cook, P., Causebrook, R., Gale, J., Michel, K., Watson, M., 2014. What Have We Learned from Small-scale Injection Projects? *Energy Procedia* **63**, 6129–6140. <https://doi.org/10.1016/J.EGYPRO.2014.11.645>
- Dean, R.H., Lo, L.L., 1988. Simulations of Naturally Fractured Reservoirs. *SPE Reservoir Engineering (Society of Petroleum Engineers)* **3**, 638–648. <https://doi.org/10.2118/14110-PA>
- Egermann, P., Bazin, B., Vizika, O., 2005. An experimental investigation of reaction-transport phenomena during CO₂ injection, in: *SPE Middle East Oil and Gas Show and Conference*, MEOS, Proceedings. Society of Petroleum Engineers, pp. 1261–1270. <https://doi.org/10.2523/93674-ms>
- Fatima, S., Khan, H.M.M., Tariq, Z., Abdalla, M., Mahmoud, M., 2021. An Experimental and Simulation Study of CO₂ Sequestration in an Underground Formations; *Impact on Geomechanical and Petrophysical Properties*, in: *Day 4 Wed, December 01*, 2021. SPE. <https://doi.org/10.2118/204726-MS>
- Grigg, R.B., Svec, R.K., 2006. CO₂ Transport Mechanisms in CO₂/Brine Coreflooding, in: *SPE Annual Technical Conference and Exhibition*. Society of Petroleum Engineers. <https://doi.org/10.2118/103228-MS>
- Hyman, Jeffrey D, Karra, Satish, Makedonska, Nataliia et al. 2015. dfnWorks: A discrete fracture network framework for modeling subsurface flow and transport. *Computers & Geosciences* **84**: 10–19.
- Keating, E., Bacon, D., Carroll, S., Mansoor, K., Sun, Y., Zheng, L., Harp, D., Dai, Z., 2016. Applicability of aquifer impact models to support decisions at CO₂ sequestration sites. *International Journal of Greenhouse Gas Control* **52**, 319–330. <https://doi.org/10.1016/J.IJGGC.2016.07.001>
- Kingma, Diederik P and Ba, Jimmy. 2014. Adam: A method for stochastic optimization. arXiv preprint arXiv:1412.6980.
- Lei, Qinghua, Latham, John-Paul, and Tsang, Chin-Fu. 2017. The use of discrete fracture networks for modelling coupled geomechanical and hydrological behaviour of fractured rocks. *Computers and Geotechnics* **85**: 151–176.

- Li, Zongyi, Kovachki, Nikola, Azizzadenesheli, Kamyar et al. 2020. Fourier neural operator for parametric partial differential equations. arXiv preprint arXiv:201008895.
- Michael, K., Golab, A., Shulakova, V., Ennis-King, J., Allinson, G., Sharma, S., Aiken, T., 2010. Geological storage of CO₂ in saline aquifers—A review of the experience from existing storage operations. *International Journal of Greenhouse Gas Control* **4**, 659–667. <https://doi.org/10.1016/J.IJGGC.2009.12.011>
- Moghadasi, J., Jamialahmadi, M., Müller-Steinhagen, H., Sharif, A., 2004. Formation Damage Due to Scale Formation in Porous Media Resulting From Water Injection, in: *Proceedings – SPE International Symposium on Formation Damage Control*. Society of Petroleum Engineers, pp. 581–591. <https://doi.org/10.2523/86524-ms>
- Mohamed, I.M., Nasr-El-Din, H.A., 2012. Formation damage due to CO₂ sequestration in deep saline carbonate aquifers, in: *Proceedings – SPE International Symposium on Formation Damage Control*. Society of Petroleum Engineers, pp. 319–350. <https://doi.org/10.2118/151142-MS>
- Mohapatra, A., Rai, C.S., Sondergeld, C.H., Richards, T., 2019. Laboratory study of ultrasonic velocity variations during CO₂ flooding in Tuscaloosa sandstone, in: *SPE Reservoir Evaluation and Engineering*. Society of Petroleum Engineers, pp. 520–530. <https://doi.org/10.2118/159515-PA>
- Müller, Sebastian, Schüller, Lennart, Zech, Alraune et al. 2022. GSTools v1. 3: a toolbox for geostatistical modelling in Python. *Geoscientific Model Development* **15** (7): 3161–3182.
- Nguyen, D.N., 2003. Carbon dioxide geological sequestration: Technical and economic reviews, in: *Society of Petroleum Engineers – SPE/EPA/DOE Exploration and Production Environmental Conference 2003, EPEC 2003*. Society of Petroleum Engineers. <https://doi.org/10.2118/81199-MS>
- Pawar, R., Bromhal, G., Carroll, S., Chu, S., Dilmore, R., Gastelum, J., Oldenburg, C., Stauffer, P., Zhang, Y., Guthrie, G., 2014. Quantification of Key Long-term Risks at CO₂ Sequestration Sites: Latest Results from US DOE's National Risk Assessment Partnership (NRAP) Project. *Energy Procedia* **63**, 4816–4823. <https://doi.org/10.1016/J.EGYPRO.2014.11.512>
- Qasem, F., Gharbi, R., Baroon, B., 2014. IPR in naturally fractured gas condensate reservoirs, in: *SPE Latin American and Caribbean Petroleum Engineering Conference Proceedings*. Society of Petroleum Engineers, pp. 435–447. <https://doi.org/10.2118/169286-ms>
- Retnanto, A., Economides, M.J., 1998. Inflow performance relationships of horizontal and multibranch wells in a solution-gas-drive reservoir, in: *Proceedings of the European Petroleum Conference*. Society of Petroleum Engineers, pp. 255–263. <https://doi.org/10.2523/50659-ms>
- Rosenbauer, R.J., Koksalan, T., Palandri, J.L., 2005. Experimental investigation of CO₂-brine-rock interactions at elevated temperature and pressure: Implications for CO₂ sequestration in deep-saline aquifers. *Fuel Processing Technology* **86**, 1581–1597. <https://doi.org/10.1016/j.fuproc.2005.01.011>
- Sadeghi, M., Shadizadeh, S.R., Ahmadi, M.A., 2013. Determination of drainage area and shape factor of vertical wells in naturally fracture reservoir with help well testing and developed IPR curve, in: *Society of Petroleum Engineers – North Africa Technical Conference and Exhibition 2013, NATC 2013*. Society of Petroleum Engineers, pp. 439–456. <https://doi.org/10.2118/164638-ms>
- Saidi, S., 1983. Simulation of Naturally Fractured Reservoirs. SPE Reservoir Simulation Symposium, in: *SPE Reservoir Simulation Symposium*. Society of Petroleum Engineers. <https://doi.org/10.2118/12270-MS>
- Shabani, B., Vilcáez, J., 2018. A fast and robust TOUGH2 module to simulate geological CO₂ storage in saline aquifers. *Comput Geosci* **111**, 58–66. <https://doi.org/10.1016/J.CAGEO.2017.10.012>
- Sharma, S.S., 2011a. Determinants of carbon dioxide emissions: Empirical evidence from 69 countries. *Appl Energy* **88**, 376–382. <https://doi.org/10.1016/J.APENERGY.2010.07.022>
- Sharma, S.S., 2011b. Determinants of carbon dioxide emissions: Empirical evidence from 69 countries. *Appl Energy* **88**, 376–382. <https://doi.org/10.1016/J.APENERGY.2010.07.022>
- Sherratt, Joseph, Haddad, Amin Sharifi, Rafati, Roozbeh et al. 2020. A fracture upscaling method (FUM) for hydraulically fractured reservoirs: From discrete fracture modelling to finite difference simulations. *Journal of Natural Gas Science and Engineering* **83**: 103611.
- Tariq, Z., Abdurraheem, A., Elkatatny, S., Mahmoud, M., Muqtadir, A., Murtaza, M., 2018a. Geomechanical Studies on CO₂ Sequestered Rocks in an Aqueous Saline Environment, in: *All Days*. SPE. <https://doi.org/10.2118/192242-MS>
- Tariq, Z., Abdurraheem, A., Khan, M.R., Sadeed, A., 2018b. New inflow performance relationship for a Horizontal well in a naturally fractured solution gas drive reservoirs using artificial intelligence technique, in: *Offshore Technology Conference Asia 2018, OTCA 2018*. Offshore Technology Conference. <https://doi.org/10.4043/28367-ms>
- Tariq, Z., Al-Hashim, H.S., Sadeed, A., Janjua, A.N., 2016. A Novel Methodology to Optimise the Parameters of Hydraulic Fracturing in Gas Condensate Reservoirs, in: *International Petroleum Technology Conference*. International Petroleum Technology Conference. <https://doi.org/10.2523/18919-ms>

- Vanorio, T., Nur, A., Diaz, E., 2011. The Rock Physicochemical Basis for Time-Lapse Seismic Reservoir Monitoring of CO₂ Injection, in: *SPE/DGS Saudi Arabia Section Technical Symposium and Exhibition*. Society of Petroleum Engineers. <https://doi.org/10.2118/149031-ms>
- Viebahn, P., Vallentin, D., Höller, S., 2015a. Prospects of carbon capture and storage (CCS) in China's power sector – An integrated assessment. *Appl Energy* **157**, 229–244. <https://doi.org/10.1016/J.APENERGY.2015.07.023>
- Viebahn, P., Vallentin, D., Höller, S., 2015b. Prospects of carbon capture and storage (CCS) in China's power sector – An integrated assessment. *Appl Energy* **157**, 229–244. <https://doi.org/10.1016/J.APENERGY.2015.07.023>
- Warren, J.E., Root, P.J., 1963. The Behavior of Naturally Fractured Reservoirs. *Society of Petroleum Engineers Journal* **3**, 245–255. <https://doi.org/10.2118/426-pa>
- Zhou, W., Wang, T., Yu, Y., Chen, D., Zhu, B., 2016. Scenario analysis of CO₂ emissions from China's civil aviation industry through 2030. *Appl Energy* **175**, 100–108. <https://doi.org/10.1016/J.APENERGY.2016.05.004>